Determination of Weld Interface Properties and their Effect on the Strength of Multi-Material Aluminium-Steel Joints

S. O. Kraus[1*], J. Bruder[1], P. Groche[1]

[1] Institute for Production Engineering and Forming Machines, TU Darmstadt, Germany
*Corresponding author. Email: stefan.kraus@ptu.tu-darmstadt.de

Abstract

Collision welding is a promising manufacturing approach for joining similar and dissimilar metals without thermally influenced strength loss. This capability unlocks new potential for lightweight construction. Among other things, components and welded joints can be made more filigree and load-optimised. Widespread industrial use of this technology is still limited by insufficient knowledge of the underlying joining mechanisms. In this paper, collision welding is applied to an aluminium-steel material combination of steel (DC04) and aluminium (AA6016). First, the welding process window for the material combination is determined on a special model test rig by varying the collision speed and the collision angle, the two main process parameters in collision welding. Shear tensile tests are then conducted to refine the weld process window, focusing on the region exhibiting the highest shear tensile strength values. Scanning Electron Microscope (SEM) images are used to analyse the weld zone, revealing the formation of four different metallographic structures in the joint zone of the welded samples. The area fractions of these structures are quantified and correlated with collision angles and corresponding shear tensile strength values.

Keywords

Collision welding, Multi-Material Design, Lightweight Concepts, Emission Reduction

1 Introduction

Mobility is a fundamental aspect of modern society, enabling access to education, healthcare and the labour market. It includes private and public transport, logistics and infrastructure (Miraftabzadeh et al., 2024). In 2023, the transport sector accounted for 21% of global CO2

emissions, 38% of which came from passenger cars (Crippa et al., 2024; EDGAR, 2024; IEA, 2025). In addition to CO2 emissions, both electric and combustion vehicles emit harmful particulate matter from brake dust and tyre abrasion, known as "non-exhaust particle emissions", which exceed exhaust particulate emissions from modern combustion engines (EEA, 2023; OECD, 2020; Lopez et al., 2023; Timmers et al., 2016). Overall up to 10% of the marine microplastics released each year originate from tyre abrasion (Kole et al., 2017; Köllner, 2024a). As a result, the Euro 7 emissions standard will regulate these emissions for the first time (ADAC, 2024; EC, 2022; Visnic, 2023).

Reducing vehicle mass is a key strategy for lowering these emissions (Bandivadekar et al., 2008; Köllner, 2024b; OECD, 2017). A 100 kg reduction in the mass of a small combustion vehicle reduces CO2 emissions by 10 g CO2/km (OECD, 2017). Increased vehicle weight has a significant impact on non-exhaust particle emissions. For example, the additional weight of 318 kg of an electric car compared to a comparable petrol car results in up to 22% higher non-exhaust particulate emissions (Beddows and Harrison, 2021). This underlines the environmental importance of lightweight design. Multi-material construction using aluminium and steel, especially in high-strength variants, supports these goals (Tisza and Lukács, 2018). However, traditional fusion welding methods such as tungsten inert gas (TIG) and laser beam welding face challenges due to the different melting points of the materials (Atabaki et al., 2014; Carlone and Astarita, 2019). If a material bond is possible at all, the melting of the materials leads to the formation of intermetallic phases in the weld zone. The associated loss of ductility in the brittle metal joints limits the potential of the materials used (Agudo et al., 2007; Khedr et al., 2023). To realise the full potential, a joining process is required that allows strong aluminium-steel joints to be made while minimising the loss of strength.

Solid-state or collision welding processes offer a solution by applying sufficiently high pressure to join similar and dissimilar materials without active heat input, avoiding the formation of intermetallic phases (Agudo et al., 2007; Kapil and Sharma, 2015; Khedr et al., 2023). Joining feasibility is defined by collision speed and angle, with the process window categorised into solid-phase, liquid-phase and hybrid joining regions (Niessen, 2022). Electromagnetic pulse welding (EMPW) facilitates collision welding in industrial settings by accelerating a joining partner via a strong electromagnetic field, creating a high-speed impact weld (Atabaki et al., 2014; Golovashchenko, 2006; Kapil and Sharma, 2015; Weddeling et al., 2010). Due to transient phenomena, the collision speed and angle dynamically vary during the course of the EMPW collision, affecting the weld properties (Stankevic et al., 2020; Wang et al., 2023). Currently, EMPW process design relies on iterative methods, which are costly and introduce uncertainties in mass production (Marschner et al., 2021). For future optimised design of EMPW processes, it is therefore necessary to know the critical angle profile for the joint design during the collision in order to best influence the achievable strength properties of the joint in a robust manner.

This study uses a mechanical collision welding test rig to analyse joint formation for the material combination DC04 with AA6016-T4 at varying collision angles and speeds. The aim is to determine the optimum angle range for joining and to correlate strength values with collision parameters. Unlike previous studies which have assessed joint strength and

microstructure at discrete points, this research uses SEM imaging to map joint structures across the weld zone and relate these findings to tensile shear strength. This should provide the basis for a future analytical model that predicts EMPW joint strength based on simulated angular profiles, thereby aiding future process optimisation.

2 Materials and Methods

The tests in this work are carried out on a model test rig for collision welding, see the brief functional description below. A detailed description of the test rig is given in (Kraus et al., 2024). The specimens used are taken from aluminium sheets (AA6016-T4, thickness: 1.5 mm, tensile strength R_m: 235 N/mm^2) and steel sheets (DC04, thickness: 2.0 mm, tensile strength R_m: 310 N/mm^2) by shear cutting. For each material, three tensile tests are performed on a *Zwick Roell 100* combined tensile and compression testing machine to determine tensile strength in accordance with DIN 50125.

The model test rig for collision welding, developed at the Institute for Production Engineering and Forming Machines (PtU) at the Technical University of Darmstadt, allows the collision welding process to be investigated over the time profile of the collision with constant and precisely adjustable collision parameters thanks to its fully mechanical design. At the same time, it offers good observability of the process and the process phenomena. Fig. 1 (a) shows the construction of the model test rig. The specimens to be welded (collision area: length × width: 12.5 mm × 12 mm) are mounted at the ends of the two rotors rotating in the same direction. The AA6016-T4 flyer specimen is pre-bent to set the collision angle β. The DC04 target is flat and is additionally supported by an anvil, see Fig. 1 (b). The collision is triggered by an engagement mechanism when the desired speed is reached, causing the specimens to collide at the position shown. The electromagnetic pulse welding (EMPW) process described in the previous section is shown in Fig. 1 (c). In contrast to the model test rig, in EMPW the flyer is accelerated towards the target by an electromagnetic field.

On the model test rig, the collision speed v_{imp} is varied in five steps of 262 m/s, 279 m/s, 305 m/s, 331 m/s and 349 m/s by rotating the rotors at a specified speed to study the transient EMPW process at discrete points. The collision angle β is varied between 3.5° and 12.5°. The specimens are cleaned with acetone immediately prior to testing to eliminate any influence on the test results from lubricant or corrosion inhibitor residues on the specimen surfaces. High-speed observation of the collision is performed using a *PCO hsfc pro* image intensifier camera, which acquires up to eight images per collision.

As shown in Fig. 1 (d), the mounting face and side edge areas of the collision welded specimens are first cut off using a wet cut-off grinder in order to remove any effects of specimen fabrication in the edge areas of the weld and to shorten the overall length (14 ± 1 mm) and width (8 ± 1 mm) of the specimen for microscopic examination in order to analyse the weld zone. The cut surfaces of the specimens are then ground on grinding and polishing machines with SiC paper (grit size P320, P400, P600, P800, P1200, P2500 and P4000) and polished with diamond suspension (3 µm and 1 µm). The weld zone is examined microscopically using a *Phenom ProX* scanning electron microscope (SEM), manufactured by *Phenom-World*. The lengths of different joint structures along the length of the weld zone

are measured with the microscope to analyse correlations between the joint structures that occur and the shear tensile strength of the welded joint. The tensile shear strength of the welded joint is determined on a *Zwick Roell 100* combined tensile and compression testing machine. For more detailed information about the tensile shear tests, see (Kraus et al., 2024).

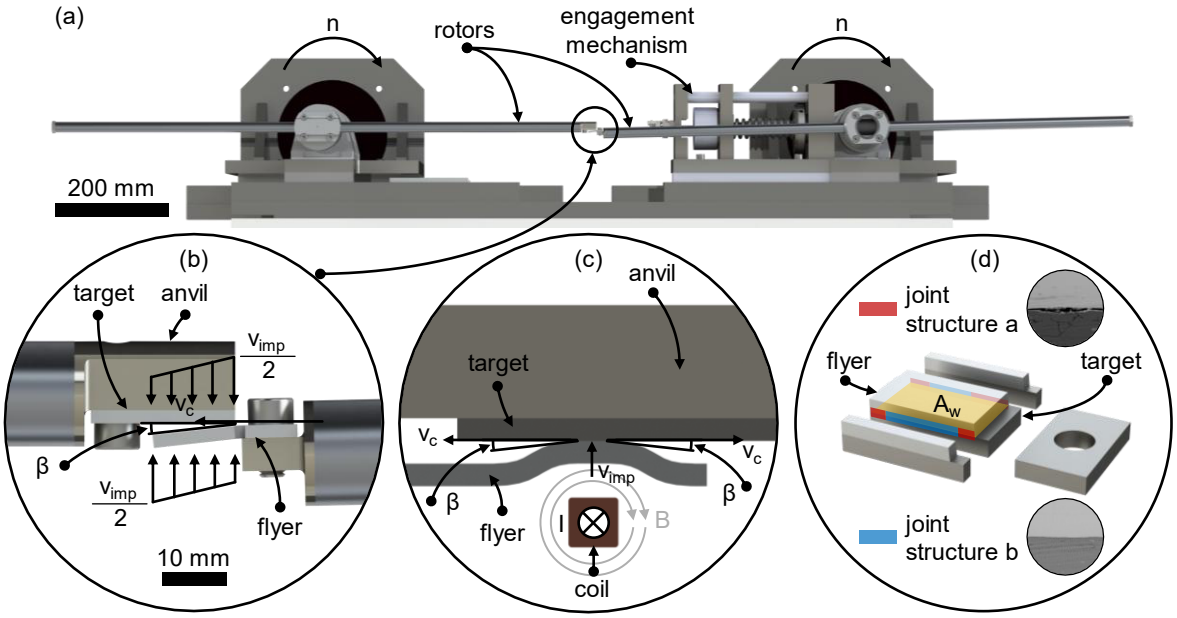

***Figure 1**: **(a)** The model test rig consists of two synchronised rotating rotors and an engaging mechanism; **(b)** The specimens are mounted at the end of each rotor (target backside supported by an anvil, flyer pre-bent to set the collision angle β); **(c)** Process setup for EMPW according to Böhme et al. (2019). The initially flat flyer is accelerated by the electric field. Collision speed v_{imp} and angle β change during the collision; **(d)** Graphic visualisation of the specimen cutting process and exemplary representation of different joint structures along the length of the weld zone.*

3 Results

3.1 Welding Process Window

The welding process window, as determined by the model test rig for the material combination of aluminium AA6016-T4 (sheet thickness 1.5 mm) and DC04 steel (sheet thickness 2.0 mm), is illustrated in Fig. 2. The collision welding tests are performed at collision speeds v_{imp} of 262 m/s, 279 m/s, 305 m/s, 331 m/s and 349 m/s. Within the defined process window, a collision weld test is considered successful if the two specimens cannot be separated by manual force after the test (black dots). For the purpose of enhancing the clarity of the diagram, the successful tests are shifted 2 m/s to the left on the collision velocity axis in comparison to the unsuccessful tests (white dots). The formation of the first bonds between the two materials occurs at a collision velocity of 305 m/s. The lower and upper limit angles at that speed are 7.3° and 8.3°, respectively. At a collision speed of 331 m/s, an

increased upper limit angle of 9.8° is determined, while the lower limit angle decreases marginally to 6.8°. Furthermore, at a collision speed of 349 m/s, an even greater increase in the upper limit angle to 11.2° is observed, whilst the lower limit angle decreases further to 6.5°.

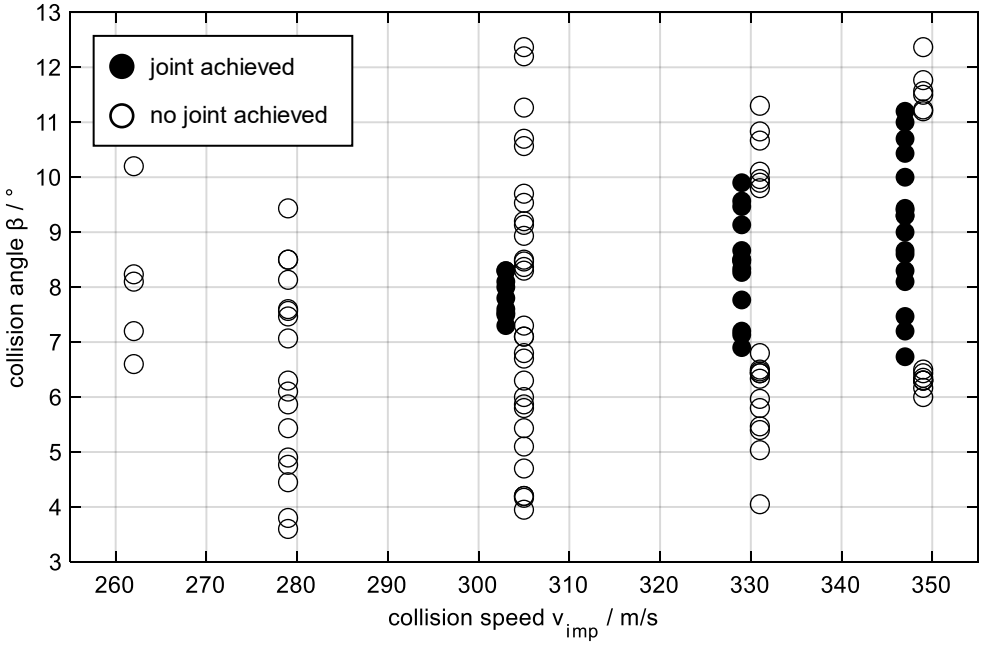

***Figure 2**: Welding process window of the material combination AA6016-T4 (flyer, thickness: 1.5 mm) and DC04 (target, thickness: 2.0 mm).*

3.2 Tensile Shear Strength of Welded Joints in the Centre of the Welding Process Window at 305 m/s, 331 m/s and 349 m/s

Following the determination of the welding process window, an investigation is conducted into whether the tensile shear strength of the collision-welded joints is dependent on the respective collision speed or whether it is independent of the collision speed. The tensile shear strength is only compared for specimens located in the centre of the process window at each of the three collision speeds (305 m/s, 331 m/s, 349 m/s). However, it should be noted that the collision angle can only be preset in 0.5° increments by pre-bending the flyer samples. Furthermore, due to the dynamics inherent in the model test rig, the rotors undergo elastic deformations, which can be attributed to various factors such as the engagement process, air resistance, and aerodynamic turbulence within the rotor protection housing. Consequently, this results in a deviation of the actual measured collision angle from the pre-set collision angle. To address this, a greater number of samples are welded at each of the three collision speeds, and then three samples are selected for each collision speed that are within a range of ±0.3° around the mean collision angle of the process window. For the process window illustrated in Fig. 2, the mean collision angle at a collision speed of 305 m/s is 7.8°. At 331 m/s, the angle is 8.3°, and at 349 m/s, 8.8°.

The tensile shear strength values obtained demonstrate an increase with increasing collision speed. Specifically, at collision speeds of 305 m/s and 331 m/s, the tensile shear strength was recorded as 22 N/mm² and 55 N/mm², respectively. For the specimens that were welded at 349 m/s, a strength of 130 N/mm² was determined. Furthermore, the specimens demonstrate divergent failure patterns during tensile shear testing. At both lower collision speeds, the welded joints shear or slide against each other in the weld zone, see Fig. 3 (a). The specimens exhibiting the highest strength demonstrate a combined failure pattern, characterised by the presence of areas along the length of the weld zone where specimens are separated by shearing or sliding against each other, and areas where shearing occurs within the aluminium material, which possesses a lower tensile strength compared to steel. Consequently, the strength of the welded joint in these areas exceeds the tensile shear strength of the aluminium material. When viewed over the length of the weld zone, shear failure in the aluminium material occurs predominantly in the middle, whereas shear or sliding in the weld zone occurs predominantly at the beginning and end, see Fig. 3 (b), (c).

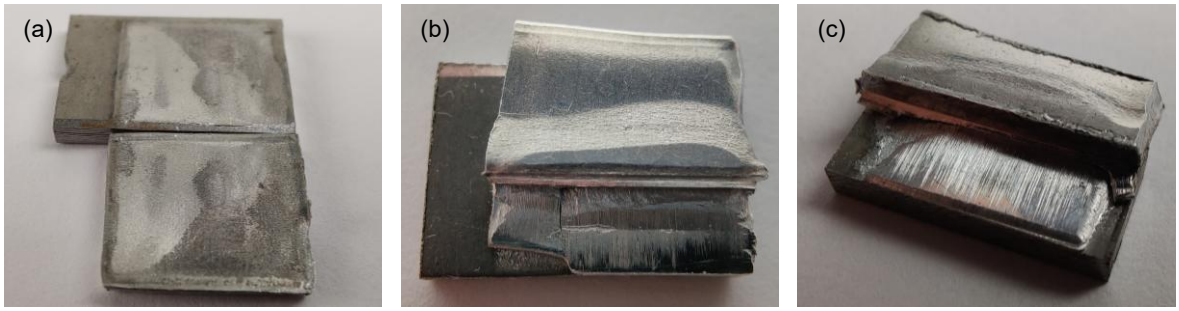

Figure 3*: Welded specimens after tensile shear testing (welding direction: right to left):* ***(a)*** *Shear or sliding failure (top: DC04, bottom: AA6016-T4);* ***(b)****,* ***(c)*** *Shear failure in the aluminium material (top: AA6016-T4, bottom: DC04).*

3.3 Joint Structures in the Weld Zone

The preceding section's investigations indicate that the welded joints produced at a collision speed of 349 m/s exhibit the highest tensile shear strength values. Further investigations are being carried out to achieve a more precise statement about the tensile shear strength over the entire angular range of the welding process window at 349 m/s. Metallographically prepared specimens (procedure described in section 2) from the entire angular range are examined in their weld zone by SEM. In instances where differing joint structures are observed along the entire length of the weld zone of the specimens, the position and length of the corresponding areas are measured, see Fig. 1 (d). These values are then used to extrapolate the area ratios of the different joint structures to the total area A_w of the welded joint. In cases where the length ratios of the structures on both sides of the specimen are unequal, the area is calculated using non-square geometries such as a trapezoid. The SEM-examinations of the weld zones reveal four distinct joint structures, as shown in Fig. 4 and briefly explained below.

The characteristic joint structure of a weld without an interlayer is shown in Fig.4 (a). The aluminium alloy AA6016-T4 (light grey) and the steel DC04 (dark grey) are located directly on top of each other. It is notable that in this structure, there is a very smooth and nearly wave-free transition zone between the two materials, with no visible voids. The structure in which an interlayer (medium grey) is present between the aluminium alloy and the steel is illustrated in the SEM image of Fig. 4 (b), (c). It is evident that the interlayer exhibits distinct variations in both colour and structure compared to the base materials. The surface of the interlayer facing the steel (the bottom of the image) is visibly smoother in comparison to the aluminium facing side, which has a much more uneven or wavy surface. In accordance with the structure depicted in Fig.4 (a), no voids were observed in the SEM images. The interlayer thickness varies between 5 µm and 30 µm, with a predominance of 10 µm. In the interlayer, lighter streaks or more sharply defined lighter areas can be seen, the colour of which is similar to that of the aluminium material.

As illustrated in Fig. 4 (d) - (f), the structures are defined by voids of differing shapes. In the following, the structure of Fig. 4 (d), (e) will be referred to as a weld zone with a cracked interlayer. It is noteworthy that the cracks manifest exclusively within the interlayer, with no evidence of such fractures in either of the two base materials. The dimensions and optical composition of the interlayer correspond to the crack-free state shown in Fig. 4 (b), (c), so that an aluminium solid solution is also assumed here only in the cracked state. In addition, the examination reveals areas where there is no bond or direct contact between the two base materials, as illustrated in Figure Fig. 4 (f). EDS (Energy Dispersive X-ray Spectroscopy) scans of a thin interlayer are shown in Fig. 4 (g).

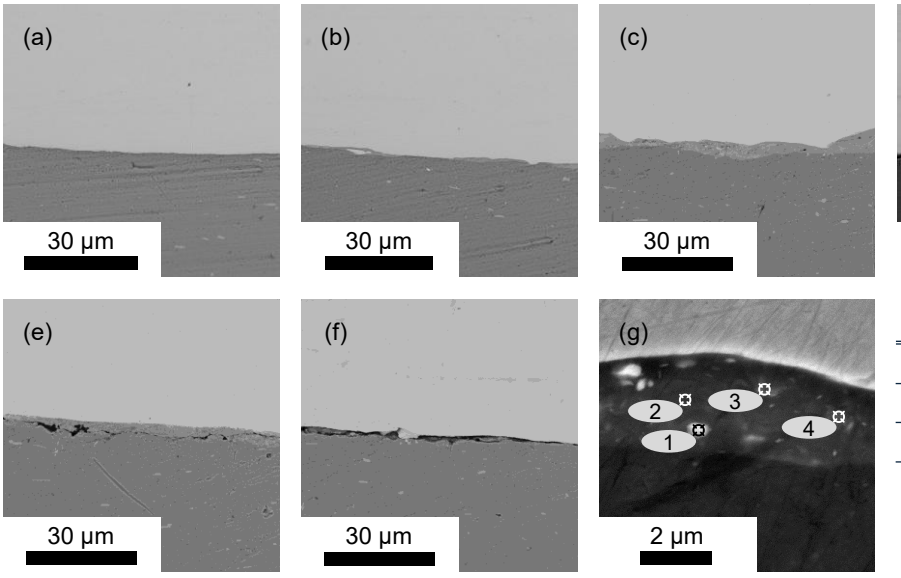

EDS	Al	Fe
1	57,6%	41,6%
2	84,6%	13,7%
3	75,2%	23,4%
4	80,6%	18,1%

***Figure 4**: SEM images of the characteristic joints structures of the weld zone (top: DC04, bottom: AA6016-T4): **(a)** Without interlayer; **(b)**, **(c)** With interlayer (medium grey, (b) thickness ≤ 3 µm, (c) thickness ≤ 10 µm); **(d)**, **(e)** With a cracked interlayer; **(f)** No contact between joining parts in the weld zone; **(g)** EDS scans of a thin interlayer.*

3.4 Tensile Shear Strength as a Function of Collision Angle

As outlined in section 3.3, the tests for the collision speed of 349 m/s are conducted on a substantially larger number of specimens, covering the full angular range of the process window. The diagram in Fig. 5 shows the curve of tensile force and crosshead travel determined with the combined tensile and compression testing machine for three specimens welded at different collision angles β at a collision speed v_{imp} of 349 m/s. The specimens with a collision angle of 7.3° and 11.2° fail after a short travel distance of the testing machine due to slipping in the welding zone, see Fig. 3 (a). The specimen with a collision angle of 9.2°, i.e., in the centre of the process window, can withstand a significantly higher maximum force. This results in failure of the welded joint due to shearing in the weaker aluminium material, see Fig. 3 (b), (c).

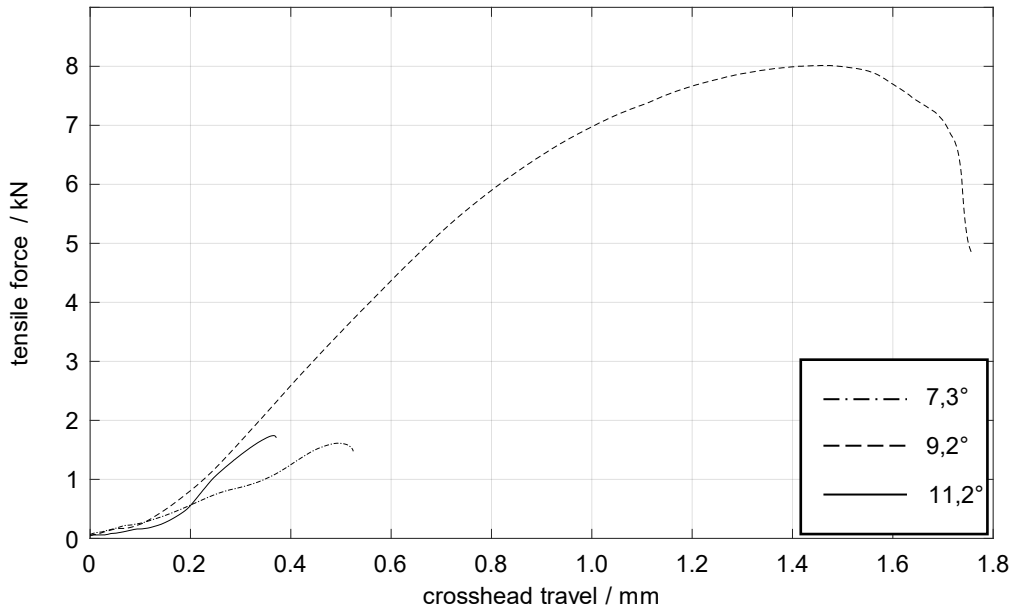

***Figure 5**: Force-travel diagram showing crosshead travel and tensile force in the tensile shear test for a collision speed of 349 m/s in dependence of the collision angle.*

A total number of 27 specimens are investigated to determine the tensile shear strength and area ratios of the joint structures (see next section 3.5). The area between the upper limit angle (11.2°) and the lower limit angle (6.5°) is divided by these 27 specimens into three angular areas. The first area I covers the angle range 6.5° - 8°, the second area II covers the angle range 8° - 10°, and the third area III covers the angle range 10° - 11.2°. The mean values for the tensile shear strength are shown in Fig. 6. The highest mean value of 131 N/mm² is observed in area II. In comparison, the strength values for area I and area III, respectively, exhibit a sharp decline towards the upper and lower limits of the process window. The lowest mean value of 30 N/mm² is measured in area I, while area III has a slightly higher mean tensile shear strength of 40 N/mm².

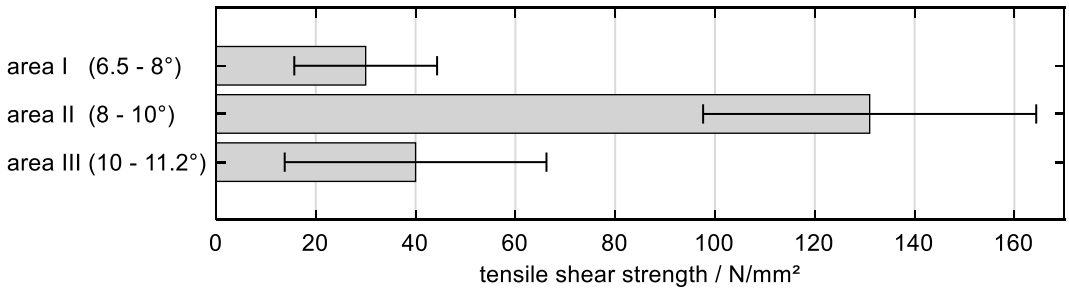

***Figure 6**: Tensile shear strength in the angular areas for a collision speed of 349 m/s.*

3.5 Area Ratios of the Joint Structures as a Function of Collision Angle

By means of the analysis of the 27 specimens using SEM, it was possible to determine the area fractions of the structures shown and described in section 3.3, utilising the procedure outlined in that same section. The results of the analysis are presented in the following diagram (Fig. 7). The diagram contains the three joint structures *weld zone without interlayer* (Fig. 4 (a)), *weld zone with interlayer* (Fig. 4 (b), (c)) and *no contact or cracked*. The latter category comprises the *weld zone with a cracked interlayer* (Fig. 4 (d), (e)) and the *no contact between joining parts in the weld zone* (Fig. 4 (f)), since neither of these structures can transfer forces in the weld zone between the aluminium and steel material. Depending on the angular area, different joint structures dominate. In area I, the *no contact or cracked* joint structure accumulates for the largest area ratio of 73%. In contrast, in areas II and III, the area ratio is comparatively reduced to 10% and 13%, respectively. The *weld zone with interlayer* dominates the joint structure in area II with a ratio of 73%. In contrast, its proportion in area I is significantly lower, at 23%, and it is absent in area III, with only 2% observed. The *weld zone without interlayer* is the dominant joint structure in area III. The area ratio of the latter increases from 4% in area I to 17% in area II and 85% in area III.

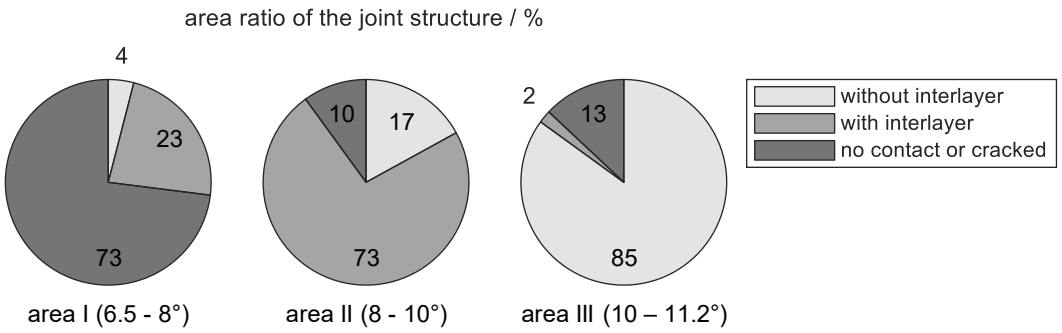

***Figure 7**: Determined area ratios of the joint structures for a collision speed of 349 m/s.*

4 Discussion

The results of this study show, at a collision speed v_{imp} of 349 m/s, a correlation between the collision angle β, the shear strength determined in tensile shear tests and the joint structures

observed in the weld zone by SEM analysis. In the lower angle range (6.5 - 8°), the weld zone is dominated by structures classified as *no contact or cracked* (Fig. 4 (d) - (f)). This can be attributed to the highly dynamic behaviour of the closing collision gap. Small angles result in high collision point velocities v_c (Fig. 1 (b)), causing the gap to close rapidly. Surface irregularities generate strong turbulence, hindering the ejection of the jet and particles and leading to gas entrapment in the weld zone (Niessen, 2022). These entrapments appear in SEM images as cracks or areas of no contact.

In the medium angle range (8 - 10°), lower collision point velocities v_c allow the jet and particles to exit the collision gap more effectively. At the same time, the conditions in the collision gap (pressure, compression of the medium in the collision gap, gas friction due to the escaping jet, etc.) still raise the temperatures high enough to allow localised melting of the base materials, resulting in a weld zone with an interlayer (Fig. 4 (b), (c)). In the upper angle range (10 - 11.2°), the temperatures are no longer sufficient to induce melting, resulting in a smooth, interlayer-free joint (Fig. 4 (a)).

The highest shear strengths were recorded in the medium angle range, despite the dominance of the interlayer in the joints of this angle range. It is assumed that the material properties of the interlayer are inferior to those of the two base materials. The high shear strength values are explained on the one hand by the low thickness of the interlayer (average thickness 10 µm), and on the other hand by the fact that the interlayer is not continuous over the length of the joint zone. However it is always present in small sections, so the interlayer does not fully express the influence of its material properties. It is also assumed that the high shear strength of the joints mentioned is due to an increase in surface area caused by the wavy interlayer, which locally interlocks the two base materials. The presence of a wavy microstructure is also associated with favourable joint properties in terms of strength in (Carpenter and Wittmann, 1975; Wittmann, 1973), among others. However, when correlating the shear strength values with the surface areas of the joint structures, it is important to note that the determined area fractions are extrapolated from only two SEM cross sections per sample. Defects located between these sections, such as central voids, may not be detected and may lead to inaccurate strength assessments.

A comparison of the observed joint structures with the characteristic joint structure zones described in (Lysak and Kuzmin, 2003) shows that the smooth interlayer-free joint typically forms in the upper angular region of the process window and shifts to larger collision angles β with increasing collision point velocity v_c. At the investigated collision speed v_{imp} of 349 m/s, this region lies at the lower threshold, which may explain the relatively low shear strength values observed (on average 40 N/mm², see Section 3.4). As shown in (Lysak and Kuzmin, 2003), higher collision velocities shift this region to larger angles, suggesting that smoother joints could achieve higher strength at higher velocities. It is expected that an increase in collision speed will increase the welding process window for the material combination of AA6016-T4 and DC04, particularly in the direction of the upper limit angle. Based on the statements in (Lysak and Kuzmin, 2003), it is also expected that at higher collision speeds for the upper angle range, the specimens with a smooth joint structure without an interlayer will have higher tensile shear strengths.

At present, these assumptions cannot be verified due to the speed limitations of the current model test rig for collision welding. A planned upgrade to a maximum speed of 500 m/s will allow more comprehensive investigations. The correlation approach introduced in this work between shear strength and area fractions of different joint structures provides a promising basis. However, future investigations will require larger sample sizes and finer angular increments to minimise statistical scatter. In the context of electromagnetic pulse welding (EMPW), such an approach can be used to simulate the transient behaviour of the collision parameters and predict the resulting joint strength.

5 Conclusions

This study comprehensively investigates the collision welding process for the material combination DC04 and AA6016-T4. Using a mechanical collision welding test rig, different collision angles are analysed to determine their effect on the formation of the joint structure of the weld zone and the tensile shear strength of the welded joints. The results show that medium collision angles (8 - 10°) at a collision speed of 349 m/s produce the most favourable welding conditions, characterised by minimal cracking and unconnected structures, resulting in higher tensile shear strength. In future research, the planned extension of the model test rig to collision speeds of 500 m/s will allow the potential further increase in weld strength at higher collision speeds to be investigated. The use of larger sample sizes and the subdivision of the angular areas into finer increments as well as a complete analysis of the welded specimens with EDX will reduce the statistical scatter and provide more detailed insights into the properties of the weld zone.

Funding

This research is a result of the project Design2Collide – Kollisionsgeschweißte Hybrid-Leichtbaustrukturen. The project is funded by the Federal Ministry for Economic Affairs and Energy (BMWE, 03LB5008H), based on a decision taken by the German Bundestag. The authors are solely responsible for the content in this publication.

Acknowledgements

The authors would like to express their thanks to Niclas Sauer. The experiments to determine the welding process window for the material combination of aluminium AA6016-T4 and steel DC04 were carried out by him as part of his master’s thesis under the supervision of Stefan Oliver Kraus and Johannes Bruder.

References

Agudo, L., Eyidi, D., Schmaranzer, C.H., Arenholz, E., Jank, N., Bruckner, J., Pyzalla, A.R., 2007. *Intermetallic Fe_xAl_y-phases in a steel/Al-alloy fusion weld*. Journal of Materials Science 42, pp. 4205-4214.

Allgemeiner Deutscher Automobil-Club e.V. (ADAC), 2024. Euro-7-Abgasnorm: Anforderungen, Grenzwerte, Einführungsfristen. Available online: https://www.adac.de/rund-ums-fahrzeug/autokatalog/abgasnormen/euro-7 (accessed on 08 April 2025).

Atabaki, M.M., Nikodinovski, M., Chenier, P., Ma, J., Harooni, M., Kovacevic, R., 2014. *Welding of Aluminum Alloys to Steels: An Overview*. Journal for Manufacturing Science and Production 14, pp. 59-78.

Bandivadekar, A., Bodek, K., Cheah, L., Evans, C., Groode, T., Heywood, J., Kasseris, E., Kromer, M., Weiss, M., 2008. On the Road in 2035: Reducing Transportation's Petroleum Consumption and GHG Emissions. Cambridge, MA, USA.

Beddows, D.C.S., Harrison, R.M., 2021. *PM10 and PM2.5 emission factors for non-exhaust particles from road vehicles: Dependence upon vehicle mass and implica-tions for battery electric vehicles*. Atmospheric Environment 244, 117886.

Böhme, M., Sharafiev, S., Schumacher, E., Böhm, S., Wagner, M.F.X., 2019. *On the microstructure and the origin of intermetallic phase seams in magnetic pulse welding of aluminium and steel*. Materialwissenschaft und Werkstofftechnik 50, pp. 958-964.

Carlone, P., Astarita, A., 2019. *Dissimilar Metal Welding*. Metals 9, 1206.

Carpenter, S.H., Wittmann, R.H., 1975. *Explosion Welding*. Annual Review of Materials Research 5, pp. 177-199.

Crippa, M., Guizzardi, D., Pagani, F., Banja, M., Muntean, M., Schaaf, E., Monforti-Ferrario, F., Becker, W., Quadrelli, R., Risquez Martin, A., Taghavi-Moharamli, P., Köykkä, J., Grassi, G., Rossi, S., Melo, J., Oom, D., Branco, A., San-Miguel, J., Manca, G., Pisoni, E., Vignati, E., Pekar, F., 2024. GHG Emissions of all World Countries, Publications Office of the European Union, Luxembourg.

EDGAR (Emissions Database for Global Atmospheric Research), 2024. IEA-EDGAR fossil CO_2 emissions. Available online: https://edgar.jrc.ec.europa.eu/report_2024#data_download (accessed on 07 April 2025).

European Commission (EC), 2022. Questions and Answers: Commission Proposal on the New Euro 7 Standards. Available online: https://ec.europa.eu/commission/presscorner/detail/en/QANDA_22_6496 (accessed on 08 April 2025).

European Environment Agency (EEA), 2023. Air Quality in Europe 2022. Available online: https://www.eea.europa.eu/publications/air-quality-in-europe-2022 (accessed on 08 April 2025).

Golovashchenko, S., 2006. Electromagnetic Forming and Joining for Automotive Applications. In: Kleiner, M. (Eds.), High Speed Forming 2006, Proceedings of the 2nd International Conference, Dortmund, Germany, pp. 201-206.

IEA, 2025. Global total final consumption by fuel in the Net Zero Scenario, 2010-2050, Paris, France. Available online: www.iea.org/data-and-statistics/charts/global-total-

final-consumption-by-fuel-in-the-net-zero-scenario-2010-2050 (accessed on 07 April 2025).

Kapil, A., Sharma, A., 2015. *Magnetic pulse welding: An efficient and environmentally friendly multi-material joining technique*. Journal of Cleaner Production 100, pp. 35-58.

Khedr, M., Hamada, A., Järvenpää, A., Elkatatny, S., Abd-Elaziem, W., 2023. *Review on the Solid-State Welding of Steels: Diffusion Bonding and Friction Stir Welding Processes*. Metals 13, 54.

Kole, P.J., Löhr, A.J., Van Belleghem, F.G., Ragas, A.M., 2017. *Wear and Tear of Tyres: A Stealthy Source of Microplastics in the Environment*. International Journal of Environmental Research and Public Health 14, 1265.

Köllner, C., 2024a. Unterschätzte Umweltgefahr Reifenabrieb. Springer Professional, available online: https://www.springerprofessional.de/fahrwerk/schadstoffe/unterschaetzte-umweltgefahr-reifenabrieb-/15490524 (accessed on 08 April 2025).

Köllner, C., 2024b. So Lassen sich Brems- und Reifenabrieb Reduzieren. Springer Professional, available online: https://www.springerprofessional.de/fahrwerk/partikel---feinstaub/so-lassen-sich-brems--und-reifenabrieb-reduzieren/18816284 (accessed on 07 April 2025).

Kraus, S.O., Bruder, J., Groche, P., 2024. *The Influence of Weld Interface Characteristics on the Bond Strength of Collision Welded Aluminium-Steel Joints*. Materials 17, 3863.

Lopez, B., Wang, X., Chen, L.W.A., Ma, T., Mendez-Jimenez, D., Cobb, L.C., Frederickson, C., Fang, T., Hwang, B., Shiraiwa, M., Park, M., Park, P., Yao, Q., Yoon, S., Jung, H., 2023. *Metal contents and size distributions of brake and tire wear particles dispersed in the near-road environment*. Science of The Total Environment 883, 163561.

Lysak, V.I., Kuzmin, S.V., 2003. Explosive Welding of Metal Layered Composite Materials. Paton Electric Welding Institute, National Academy of Sciences of Ukraine, Kiev, Ukraine.

Marschner, O., Pabst, C., Schäfer, R., Pasquale, P., 2021. Suitable Design for Electromagnetic Pulse Processes. In: High Speed Forming 2021, Proceedings of the 9th International Conference, Dortmund, Germany, pp. 1-9.

Miraftabzadeh, S.M., Longo, M., Foiadelli, F., 2024. Mobility and Future Trends. In: Passerini, S., Barelli, L., Baumann, M., Peters, J.; Weil, M. (Eds.), Emerging Battery Technologies to Boost the Clean Energy Transition, Springer, Cham, Switzerland, pp. 3-11.

Niessen, B., 2022. Untersuchungen zur Robustheit von Kollisionsschweißprozessen bei minimalem Energieeintrag. Ph.D. thesis, TU Darmstadt, Darmstadt, Germany.

Organisation for Economic Co-Operation and Development (OECD) The International Transport Forum, 2017. Lightening Up: How Less Heavy Vehicles Can Help Cut CO2 Emissions. Available online: https://www.itf-oecd.org/less-heavy-vehicles-cut-co2-emissions (accessed on 07 April 2025).

Organisation for Economic Co-Operation and Development (OECD), 2020. Non-Exhaust Particulate Emissions from Road Transport. Available online: https://doi.org/10.1787/4a4dc6ca-en (accessed on 08 April 2025).

Stankevic, V., Lueg-Althoff, J., Hahn, M., Tekkaya, A.E., Zurauskiene, N., Dilys, J., Klimantavicius, J., Kersulis, S., Simkevicius, C., Balevicius, S., 2020. *Magnetic Field Measurements during Magnetic Pulse Welding Using CMR-B-Scalar Sensors*. Sensors 20, 5925.

Timmers, V.R.J.H., Achten, P.A.J., 2016. *Non-exhaust PM emissions from electric vehicles*. Atmospheric Environment 134, pp. 10-17.

Tisza, M., Lukács, Z., 2018. *High strength aluminum alloys in car manufacturing*. IOP Conference Series: Materials Science and Engineering 418, 012033.

Visnic, B., 2023. Europe's Dust Buster. SAE International, available online: https://www.sae.org/news/2023/05/brakes-sustainability-dust-regulations (accessed on 08 April 2025).

Wang, X., Li, C., Zhou, Y., Xu, C., Dai, M., 2023. *Mechanism of the discharge behavior in electromagnetic pulse welding: Combination of electron emission and electric field*. Materials Today Communications 36, 106726.

Weddeling, C., Woodward, S., Nellesen, J., Psyk, V., Marré, M., Brosius, A., Tekkaya, A.E., Daehn, G.S., Tillmann, W., 2010. Development of design principles for form-fit joints in lightweight frame structures. In: Babusci, K., Daehn, G., Marré, M., Tekkaya, A.E., Weddeling, C., Zhang, Y. (Eds.), High Speed Forming 2010, Proceedings of the 4th International Conference, Columbus, OH, USA, pp. 137-148.

Wittman, R.H., 1973. The influence of collision parameters of the strength and microstructure of an explosion welded aluminium alloy. In: Proceedings of the 2nd International Symposium on Use of an Explosive Energy in Manufacturing Metallic Materials, pp. 153-168.